Analysis and Compensation of Phase Noise in FMCW LiDAR Sensors

Javier Pérez Santacruz, Jac Romme, Xuebing Zhang, Esteban Venialgo Araujo,
Marcus Dahlem, *Senior Member, IEEE*, and Ruud M. Oldenbeuving

***Abstract*—Light detection and ranging (LiDAR) sensors bring remarkable features to the automotive industry, enabling the development of autonomous vehicles. More concretely, frequency-modulated continuous-wave (FMCW) light detection and ranging (LiDAR) sensors offer several advantages over their time-of-flight (ToF) counterparts in terms of maximum achievable distance, interference immunity, and velocity detection. Nonetheless, FMCW LiDAR systems are inevitably affected by phase noise, limiting the sensor performance. One evident solution consists in using narrow linewidth lasers, at the expense of overall sensor cost. Therefore, in this work, a thorough analysis of the phase noise is conducted for FMCW LiDAR sensors. Moreover, a novel and low-complex phase noise compensation algorithm based on pre-estimation and feedforward correction (PNC-PEFC) is proposed. The PNC-PEFC algorithm is extensively evaluated in an experimental setup under different target distances and additive white Gaussian noise (AWGN) conditions. The experimental results show excellent performance when applying the proposed PNC-PEFC algorithm, proving its robustness across all evaluated conditions.**

***Index Terms*—Automotive, autonomous vehicles, feedforward correction, FMCW, LiDAR, OPLL, phase noise, 3D sensor.**

I. INTRODUCTION

AUTONOMOUS vehicles will bring unprecedented benefits to society such as safer roads, quicker commute times, improved logistics, less pollution, and reduced transportation cost [1]. In automotive scenarios, foggy, rainy, and dark conditions complicate the reliability of vehicle sensors, especially for long-distance detection [2]. Additionally, the diverse variety of automotive scenarios requires rapid and high-resolution scene scans for effective decision-making. Therefore, autonomous vehicles must be able to accurately sense the 3D environment with high-resolution, speed, and reliability. Nowadays, radars and cameras are the most worldwide used sensors in the automotive industry for mid- and long-distance detection (up to $\approx 250\,\mathrm{m}$) [3], [4], [5]. However, radar sensors suffer from limited angular resolution compared to cameras, primarily due to the use of relatively long wavelengths. On the other hand, cameras are hindered by their dependency on ambient light and their inaccuracies in detecting targets at long distances. Hence, light detection and ranging (LiDAR) emerges as a promising and complementary sensing technology, allowing for long-distance 3D scans with exceptionally fine angular resolution.

LiDAR and radar sensors are active technologies that enable accurate detection of targets at further distances compared to other sensing technologies like cameras [3]. Moreover, LiDAR operates on a principle similar to radar, with the differentiation that LiDAR utilizes wavelengths in the optical domain. As a consequence, compared to radar, LiDAR enables finer angular resolution, on the order of centidegrees, while keeping a relatively small size [6]. Nonetheless, the use of shorter wavelengths inherently leads to higher signal degradation in adverse weather conditions because these wavelengths are more susceptible to interference from ambient particles [7]. Thereby, to achieve effective sensing, radar and LiDAR data should be fused, leveraging the strength of both sensors: high-resolution of LiDAR and great reliability of radar [8].

There are two main types of LiDAR technologies: time-of-flight (ToF) and frequency-modulated continuous-wave (FMCW). ToF LiDAR operates on incoherent detection, while FMCW LiDAR uses a coherent approach. The coherent aspect of FMCW LiDAR brings attractive benefits such as inherent velocity detection, and extended detection range [2]. However, the use of coherent detection inevitably leads to a susceptibility to phase noise impairment which mainly occurs in the laser. This phase noise impairment limits the maximum detectable range to the coherence length of the laser. Although laser implementations on-chip, such as external cavity diode lasers (ECDLs), are unrivaled in their combination of fabrication cost, footprint and low-linewidth performance, the downside is complexity in design, laser control, and need for high-cost low-noise electronics to achieve optimal performance [9].

An alternative to using ultra-narrow linewidth integrated lasers consists in utilizing a relatively low-cost, lower-quality laser and employ phase noise compensation methods to increase performance. In the literature, there are two main approaches for phase noise compensation in FMCW LiDAR systems: optical phase-locked loop (OPLL) and feedforward correction [10], [11], [12], [13], [14], [15]. Both phase noise compensation methods use an optical delay line to extract the phase noise. OPLL realizes the phase noise compensation using a feedback mechanism, whereas the feedforward approach operates in an

Received 9 December 2024; revised 25 February 2025; accepted 14 March 2025. Date of publication 17 March 2025; date of current version 16 June 2025. This work was supported by the PhotonDelta National Grow Fund programme – www.photondelta.com. *(Corresponding author: Javier Pérez Santacruz.)*

Javier Pérez Santacruz, Jac Romme, Xuebing Zhang, Esteban Venialgo Araujo, and Ruud M. Oldenbeuving are with the IMEC-NL Holst Centre, 5656 AE Eindhoven, The Netherlands (e-mail: perezs54@imec.be).

Marcus Dahlem is with the IMEC, 3001 Leuven, Belgium.

Color versions of one or more figures in this article are available at https://doi.org/10.1109/JLT.2025.3552237.

Digital Object Identifier 10.1109/JLT.2025.3552237

open-loop configuration. Because of this loop distinction, the performance of OPLL is highly influenced by the loop delay. Thereby, OPLL requires accurate and rapid phase noise estimation. There is a trade-off between loop delay and phase noise estimation accuracy, which constrains the OPLL performance in terms of phase noise compensation [12], [13], [14].

In contrast, the feedforward phase noise compensation approach is not limited to the loop delay. In this case, more sophisticated methods can be utilized for phase noise compensation without time constraints. Previous research has explored the feedforward phase noise compensation approach in different applications such as optical frequency domain reflectometry (OFDR), being an investigation gap for automotive FMCW LiDAR systems. In [16], a digital signal processing (DSP) algorithm is proposed for phase noise compensation in an FMCW LiDAR setup using the feedforward approach. However, this DSP algorithm employs brute force, being unfeasible for real-time implementation. For this reason, this work proposes a novel, high-performance, and low-complexity phase noise compensation algorithm based on pre-estimation and feedforward correction (PNC-PEFC) for FMCW LiDAR systems. With the presented phase noise compensation method, the FMCW LiDAR technology becomes more affordable, as it allows for the use of relatively inexpensive lasers and facilitates mass production.

It is relevant to note that the proposed PNC-PEFC algorithm is only applicable to static targets and single-target detection. Nevertheless, the PNC-PEFC algorithm can be easily extended to dynamic single-target scenarios, where the up- and down-ramp signals need to be jointly processed [17]. Thereby, this manuscript is structured as follows: Section II explains, models, and analyzes the phase noise in FMCW LiDAR systems. Section III presents the novel PNC-PEFC algorithm for phase noise compensation, offering both high phase noise reduction and low-complexity. Section IV demonstrates and quantifies the performance of the proposed PNC-PEFC algorithm in an experimental FMCW LiDAR setup under different target distances. Finally, Section V summarizes the main contributions and conclusions of this work.

II. PHASE NOISE ANALYSIS IN FMCW LIDAR SYSTEMS

Phase noise impairment dwells on an undesired phase fluctuation $\varphi(t)$, which follows a continuous-time stochastic process. Phase noise is typically expressed in terms of linewidth, which specifies the full width at half-maximum (FWHM) of the optical carrier spectrum. In automotive FMCW LiDAR systems, the phase noise sources are diverse and of different nature, including intrinsic laser linewidth β_{int}, electrical noise from the laser driver, temperature fluctuations, mechanical vibrations, and dynamic changes in the laser. The contribution of all these phase noise sources determines the effective linewidth β_{eff} of the FMCW LiDAR system.

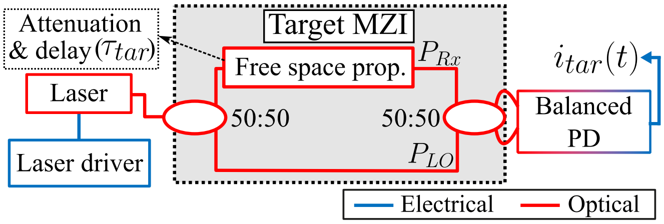

Fig. 1. Basic schematic for representing the phase noise impairment in an FMCW LiDAR system.

Fig. 1 shows a simplified schematic of an FMCW LiDAR system. First, the laser generates a linear chirp by using direct modulation. Later, the optical chirp signal passes through a Mach–Zehnder interferometer (MZI). The upper MZI branch is attenuated and delayed with respect to the lower branch, with τ_{tar} representing the two-way target delay. In FMCW LiDAR sensors for automotive applications, these attenuation and delay processes emulate the free-space propagation of the emitted optical signal. Finally, the reference signal from the lower MZI branch is combined and mixed with its delayed and attenuated version in a balanced photodetector (BPD). Assuming perfect balancing, the resulting electrical signal after the BPD beating can be formulated as follows [18], [19]:

$$i_{tar}(t) = \left(R\sqrt{P_{Rx}P_{LO}}\right) \cdot \sin\left(\omega_{beat}t + \Delta\varphi(t,\tau_{tar})\right) + z(t), \tag{1}$$

where R is the responsivity of the BPD. P_{Rx} and P_{LO} are the local oscillator (LO) and received powers, respectively. The term $z(t)$ refers to additive noise from sources such as dark or shot noises of the BPD. Moreover, ω_{beat} is the beat angular frequency, linearly proportional to the upper delay τ_{tar} shown in Fig. 1 [20]. In Eq. (1), the term $\Delta\varphi(t,\tau_{tar})$ represents the phase noise difference between the two branches depicted in Fig. 1: $\varphi(t) - \varphi(t,\tau_{tar})$. In other words, the phase noise level of the beat signal is proportional to the effective linewidth β_{eff} of $\varphi(t)$ and the delay difference τ_{tar} between the two MZI branches.

A portion of the phase noise signal $\varphi(t)$ is originated from the laser intrinsic linewidth, which is typically modeled as a Wiener process in the time domain [21]. Assuming that $\varphi(t)$ follows a Wiener process, the power spectral density (PSD) of the current signal $i_{tar}(t)$ without the $z(t)$ term at baseband can be expressed by the following equation [18], [19]:

$$S(\omega,\tau_{tar},T) = T\,\mathrm{sinc}^2\left(\frac{T\omega}{2}\right)\exp\left(\frac{-2\tau_{tar}}{\tau_c}\right) + \frac{\tau_c}{1+\left(\frac{\omega\tau_c}{2}\right)^2} \cdot \\ \cdot\left\{1 - \exp\left(\frac{-2\tau_{tar}}{\tau_c}\right)\left[\cos(\omega\tau_{tar}) + \frac{2}{\omega\tau_c}\sin(\omega\tau_{tar})\right]\right\}, \tag{2}$$

where T is the time window during which the spectrum is calculated, and τ_c is equal to $1/(\pi\beta_{int})$. In Eq. (2), it is assumed that $T \gg \tau_{tar}$ and $T \gg \tau_c$. Equation (2) contains two additive terms. The first additive term corresponds to the beat signal level, while the second term is denominated as pedestal noise, which follows a quasi-Lorentzian function [19], [22]. As the delay τ_{tar} increases, the beat signal level decreases and the pedestal noise level rises. When the beat signal level exceeds the pedestal noise level, the FMCW LiDAR system is considered to be operating in the coherent regime. At this point, the signal-to-noise ratio

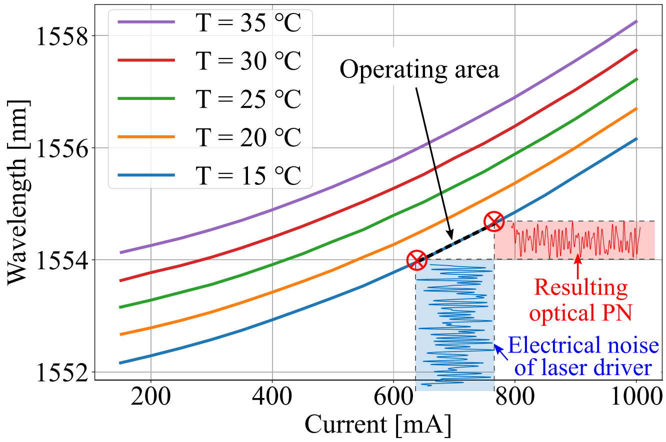

Fig. 2. Laser wavelength curve as a function of the applied current for various operational temperatures. These curves are extracted from the datasheet of the DFB1550P Thorlabs laser. Notes: the red crossing points delineate the modulation range; PN stands for phase noise; the electrical noise is exaggerated because of representation matters.

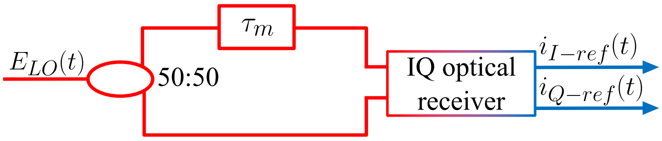

Fig. 3. Scheme of the phase noise reference branch.

(SNR) of the beat signal in Eq. (1) can be derived and formulated as follows [19]:

$$SNR = \frac{T_{chirp} R P_{Rx} \exp(\frac{-2\tau_{tar}}{\tau_c})}{2e + R P_{Rx}\tau_c \left[1 - \exp(\frac{-2\tau_{tar}}{\tau_c})(1 + \frac{2\tau_{tar}}{\tau_c})\right]}, \quad (3)$$

where e is the elementary charge and T_{chirp} corresponds to the chirping period. It is important to mention that the SNR formula in Eq. (3) assumes that P_{LO} is sufficiently high so that the shot noise originating from the photodetection process becomes the main contributor to the additive term $z(t)$ in Eq. (1). Moreover, in Eq. (3), τ_c is considered to be non-zero due to the asymptotic limit. One can notice that the mentioned additive terms of Eq. (2) are represented in the numerator and denominator of Eq. (3), respectively. As a conclusion, the performance of FMCW LiDAR systems is limited by both shot and phase noises, as quantified in Eq. (3).

A major contributor to the final phase noise is the electrical noise from the laser driver. In other words, the bias current applied to the laser is not perfectly constant, exhibiting fluctuations. As a consequence, phase noise originates from these current fluctuations and its levels depend on the wavelength-current curve of the employed laser. Fig. 2 illustrates an example of this curve for the Thorlabs distributed-feedback (DFB) laser, model DFB1550P [23]. As observed in Fig. 2, the laser wavelength depends on the applied current and the operational temperature.

In the particular example of Fig. 2, the slope of the curves increases as the applied current rises. Therefore, the phase noise induced by the electrical noise of the laser driver increases at higher applied current values (see signal representation in Fig. 2). In parallel, the laser output power is proportional to the applied current. Hence, there is an evident trade-off between high laser output power and sensitivity to laser driver induced phase noise. By observing Eq. (3), it is clear that increasing the laser power directly enhances the received power P_{Rx} and, consequently, boosts the SNR. However, as introduced above, in certain laser implementations, higher laser power is associated with increased phase noise. Higher phase noise deteriorates the SNR level, as indicated in Eq. (3). In these cases, an elegant approach to optimize the SNR consists in operating in the maximum power output regime of the laser and performing phase noise compensation. Additionally, in other FMCW optical source implementations, phase noise often sacrifices for higher power stability, tighter integration, and/or increased linewidth leading to higher output power. Consequently, in these cases, phase noise compensation becomes essential to enhance the SNR.

III. PROPOSED PNC-PEFC ALGORITHM FOR PHASE NOISE COMPENSATION IN FMCW LIDAR SYSTEMS

Before implementing phase noise compensation, it is necessary to extract a phase noise reference signal. Fig. 3 illustrates a block diagram of the required hardware for obtaining this phase noise reference signal. The phase noise reference branch in Fig. 3 is fed with a portion of the FMCW optical signal corrupted by phase noise ($E_{LO}(t)$). Next, the LO signal passes through an MZI, where the delay τ_m between the two branches is defined and known. Lastly, the signals from the MZI branches are combined and beat in an in-phase and quadrature (IQ) optical receiver. Opting for an IQ optical receiver is strongly recommended over a single BPD, since it enables more accurate phase extraction. If a single BPD is employed instead of an IQ optical receiver, a Hilbert transform is required, resulting in less precise phase extraction [16]. This imprecision becomes more critical when ω_{beat} is close to DC because the Hilbert transform internally realizes a dual filtering process to separate negative and positive frequencies, where the filter edges overlap in the DC.

Using the optical hardware structure shown in Fig. 3, the phase noise difference at τ_m, denoted as $\Delta\varphi(t, \tau_m)$, can be continuously measured. In OPLL implementations, the original phase noise signal $\varphi(t)$ needs to be estimated from $\Delta\varphi(t, \tau_m)$. In the literature, the proportional–integral–derivative (PID) procedure is commonly used for this $\varphi(t)$ estimation [24]. In the context of feedforward phase noise compensation, estimating the phase noise difference at the target distance, expressed as $\Delta\varphi(t, \tau_{tar})$, is necessary. For estimating the phase noise difference, the concatenately generated phase (CGP) method is employed, using the following equation [25]:

$$\Delta\varphi(t, k\tau_m) = \sum_{p=0}^{k-1} \Delta\varphi(t - p\tau_m, \tau_m), \quad (4)$$

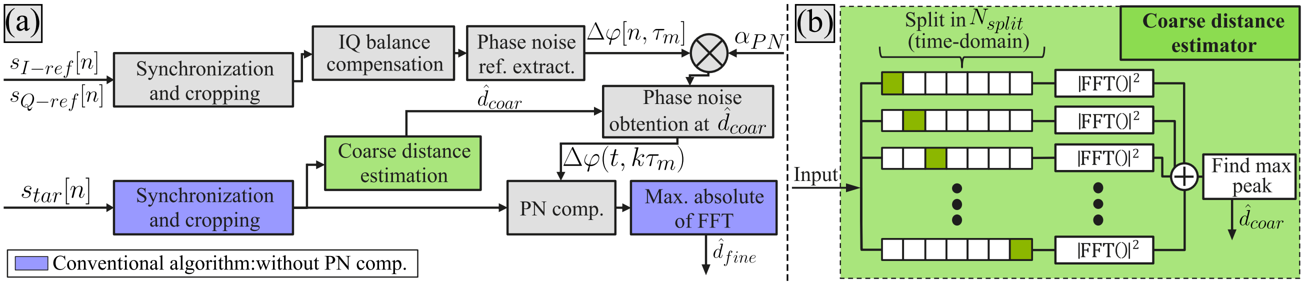

Fig. 4. Proposed PNC-PEFC algorithm for single-target detection in automotive FMCW LiDAR systems: (a) complete algorithm; (b) coarse distance estimation algorithm based on splitting periodogram process. Note: the conventional distance estimator algorithm is represented with blue blocks.

where k is an integer number. The value of k of Eq. (4) is calculated as follows:

$$k = \text{round}\left(\frac{\tau_{tar}}{\tau_m}\right). \tag{5}$$

Inspecting Eq. (4), it is worth noting that when τ_{tar} is not multiple of τ_m, there is a residual phase noise which is proportional to the rounding remainder in Eq. (5). Therefore, ideally, τ_m should be as small as possible to minimize this residual phase noise. Nevertheless, reducing τ_m leads to two negative side-effects:

- The effectiveness of phase noise compensation deteriorates more when errors occur in the phase noise extraction of $\Delta\varphi(t,\tau_m)$ as this demands additional extrapolations using Eq. (4).
- Inaccuracy in the extraction of $\Delta\varphi(t,\tau_m)$ typically originates non-desired peaks in the frequency domain, appearing near the target beat peak with a periodicity proportional to the beat frequency of τ_m. In addition, more non-desired peaks emerge when τ_m is lower. As a consequence, discarding these non-desired peaks becomes more complex for low values of τ_m.

Furthermore, the physical length of the delay line in the MZI phase noise reference branch scales proportionally with τ_m. Therefore, for the realization of an FMCW LiDAR sensor integrated in a photonic integrated circuit (PIC), a low value of τ_m is preferred in order to miniaturize the optical delay line. As a conclusion, the value of τ_m plays a crucial role in the phase noise compensation based on feedforward correction, whose value determines a trade-off between PIC size, DSP complexity, and phase noise compensation performance.

Fig. 4 shows the proposed PNC-PEFC algorithm for automotive FMCW LiDAR sensors. The inputs of the PNC-PEFC algorithm are the target beat and reference phase noise signals. These input signals correspond to the outputs of the schematics in Figs. 1 and 3, respectively, after electrical amplification and digitization. First, in the PNC-PEFC algorithm, the input signals are synchronized and cropped. Synchronization is carried out via a trigger signal from the laser driver, which indicates the instant to initiate acquisition in the analog-to-digital converter (ADC) or oscilloscope. The synchronization process is important because phase noise evolves over time. For proper phase noise compensation, any synchronization error should remain two or three orders of magnitude smaller than $1/\beta_{eff}$. In other words, if the reference complex signal $s_{ref}[n]$ and the target signal $s_{tar}[n]$ are not well synchronized, the phase noise of both signals is less correlated.

The upper branch of Fig. 4(a) estimates the phase noise of the target signal $s_{tar}[n]$, while the lower branch realizes phase noise compensation. In the upper branch, $s_{I-ref}[n]$ and $s_{Q-ref}[n]$ are balanced in terms of phase and amplitude, since the IQ optical receiver is not an ideal component and introduces phase shifting and amplitude mismatch. The IQ balance block is essential for effective phase noise compensation and must continuously compensate for both amplitude and phase, as mismatches in these parameters evolve during time. Subsequently, the phase noise reference signal $\Delta\varphi[n,\tau_m]$ is obtained by performing angle and unwrap operations on the balanced IQ signals [16]. This phase noise reference signal is then scaled by a constant factor α_{PN}. The value of α_{PN} ranges from zero to one, which allows for a gradual increase in the amount of phase noise compensation being applied. In Section IV, different values of α_{PN} are evaluated in order to quantify their impact on the final performance of the PNC-PEFC algorithm.

Next, $\Delta\varphi[n,k\tau_m]$ needs to be calculated. However, the value k is unknown a priori. Therefore, in parallel, a coarse distance estimation is performed in the lower branch of Fig. 4(a). This coarse distance estimation must be robust under additive white Gaussian noise (AWGN) conditions. Thereby, a coarse distance estimator based on the periodogram functionality is proposed, as illustrated in Fig. 4(b) [26]. In this coarse distance estimator, the target beat signal is split into N_{split} equal parts. Subsequently, the fast Fourier transform (FFT) and the absolute square operations are individually realized for each time signal segment. Finally, the absolute square signals are summed and the coarse distance value is extracted from the maximum peak of this summation. The advantage of this periodogram-based process is that the AWGN floor noise is smoothed through averaging [26]. Nonetheless, this periodogram process results in a reduced range resolution since the effective excursion frequency is diminished [16]. Nevertheless, since this periodogram process serves as a coarse distance estimator, the aforementioned reduction in range resolution does not significantly impact the final performance of the PNC-PEFC algorithm when N_{split} is not excessively high.

The value of k can then be obtained using Eq. (5) and the coarse estimated distance $\hat{d}_{coar}$. Next, the phase noise signal $\Delta\varphi[n,k\tau_m]$ can be calculated by employing Eq. (4) and be used

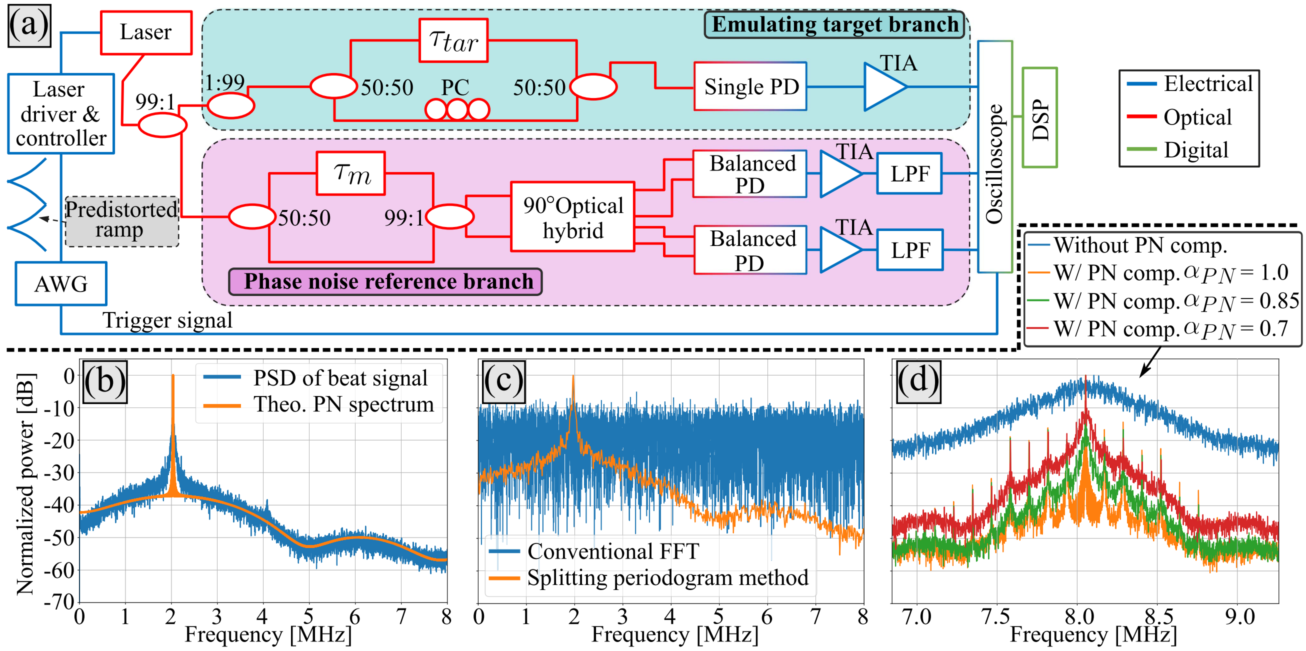

Fig. 5. Experimental FMCW LiDAR setup and results for evaluating the proposed PNC-PEFC algorithm: (a) schematic of the experimental setup; (b) PSDs of beat signal with 70 m of optical delay line together with PSDs of phase noise theoretical formula of Eq. (2) with 110 kHz of linewidth (β_{int}); (c) beat signal spectrum by using conventional FFT versus by using the splitting periodogram method of Fig. 4(b) (SNR = 14 dB); (d) periodogram of 10 up-ramp frames with and without phase noise compensation and sweeping the value of α_{PN}. Note: the pair of numbers closed to the optical splitters indicates the percentage of power from the input to the upper and lower outputs, respectively.

for phase noise compensation in the synchronized and cropped target beat signal. It is worth mentioning that the phase noise compensation block performs the following operation:

$$s_{PN-comp}[n] = s_{in}[n] \cdot \exp(\pm j\Delta\varphi[n, k\tau_m]), \qquad (6)$$

where the sign of the complex exponential argument is negative for the up-ramp and positive for the down-ramp. After the phase noise compensation process in the time domain, FFT and absolute operations are realized. Ultimately, the maximum peak frequency of the obtained absolute FFT signal is utilized to determine the target distance, getting $\hat{d}_{fine}$. It is noteworthy that if the processing time of the PNC-PEFC algorithm, presented in Fig. 4, is shorter than T_{chirp}, the response time of the LiDAR sensor remains unaffected by the added phase noise compensation method. Overall, the algorithm of Fig. 4 enables low-complexity phase noise compensation for single-target detection under AWGN and phase noises conditions, and its performance is experimentally evaluated in Section IV.

IV. EXPERIMENTAL SETUP AND RESULTS

Fig. 5(a) shows the experimental setup for evaluating the PNC-PEFC algorithm. First, FMCW generation is achieved through direct modulation. The employed optical source is a DFB laser from Thorlabs, model DFB1550P [23]. The CTL200 B-600 board from Koheron is utilized to drive and control this laser. The laser bias current is set to 650 mA, providing an optical output power of 100 mW, which is the specified maximum power that this laser can deliver. As commented in Section II, for the DFB1550P laser, higher bias currents result in increased phase noise (see Fig. 2). The generated FMCW signal has a bandwidth of 3 GHz, providing a range resolution of 5 cm. This range resolution value is sufficient for automotive scenarios [5].

A triangular waveform with a voltage amplitude range of 1.06 V is used to obtain the aforementioned 3 GHz bandwidth in the FMCW optical signal. This voltage waveform is generated by using the Tektronix arbitrary waveform generator (AWG) AFG3252, which operates at a sampling rate of 2 GSa/s and 14 bits of resolution. As illustrated in Fig. 5(a), the triangular waveform is pre-distorted since the wavelength/current curves shown in Fig. 2 are not linear, following a similar process described in [20] and [27]. As a result, an FMCW optical signal centered at approximately 1555 nm with a bandwidth of 3 GHz is generated. The optical output of the laser is measured without modulation using the linewidth analyzer LWA-1 k series from HighFinesse, resulting in an effective linewidth β_{eff} of approximately 900 kHz. Furthermore, the full chirp period ($2 \cdot T_{chirp}$) for combined up- and down-ramps is 1000 μs. 95 % of the central part of the up- and down-ramps is utilized as the region of interest (ROI) because the pre-distorted triangular waveform is more abrupt and inaccurate at its edges [20].

The generated FMCW signal is split into two branches: one emulating the target and the other serving as the phase noise reference. The emulating target branch aims to replicate the delay difference between the LO and received signals. This delay difference, represented as τ_{tar}, is achieved by utilizing optical patch cords of varying lengths, equivalent to the setup illustrated in Fig. 1. In the lower branch of the target MZI, a polarization controller (PC) is used to align the polarization of both signal arms. Then, the combined optical signals pass through the receiver block chain, which consists of a single photodetector (PD) followed by a transimpedance amplifier (TIA). The 40 GHz PD module from Shenzhen is employed for this receiver block chain.

On the other hand, the phase noise reference branch aims to acquire phase noise information in every up- and down-ramps. This phase noise reference branch corresponds to the scheme depicted in Fig. 3. The selected optical fiber length for the τ_m delay is $4\,\mathrm{m}$, since this value provides a good balance between phase noise compensation performance and chip area. Moreover, the COH090-SP-U component from iXblue is used as the 90° optical hybrid. It is important to mention that the optical components in the phase noise branch are polarization maintaining. The I and Q signals pass through the PDB570C module from Thorlabs, which contains a BPD followed by a TIA and a $400\,\mathrm{MHz}$ bandwidth low-pass filter (LPF). It is essential that the components of the I and Q arms are equivalent for proper phase extraction. Thus, the three electrical signals from both branches are captured with the MSOX 3024A oscilloscope from Keysight, applying a sampling rate of $50\,\mathrm{MSa/s}$. The sampling rate of the oscilloscope's ADC determines the maximum linewidth to compensate for [11]. Also, a synchronization signal from the AWG serves as trigger event in the oscilloscope acquisition process. Finally, the obtained digital signals are used as inputs in the proposed PNC-PEFC algorithm of Fig. 4.

Fig. 5(b) represents the periodogram of 10 target beat signals, using a $70\,\mathrm{m}$ optical delay line τ_{tar}. In Fig. 5(b), the theoretical PSDs of the phase noise, as formulated in Eq. (2), is also plotted, considering an intrinsic linewidth β_{int} of $110\,\mathrm{kHz}$. The experimental and theoretical PSDs match well at frequencies distant from the beat frequency ω_{beat}. However, for frequency components near the beat frequency, the experimental and theoretical PSDs do not match because the experimental PSD suffers from a quasi-Gaussian shape at these frequencies. This quasi-Gaussian shape mainly results from phase noise induced by the electrical noise of the laser driver, as previously explained in Section II. More specifically, the employed Koheron laser driver suffers from low-frequency electrical noise. This fact explains why the quasi-Gaussian shape extends across low-frequency components near the beat frequency. Furthermore, it is observed that the width of the mentioned quasi-Gaussian shape is proportional to the difference delay τ_{tar} of the the target MZI. As a conclusion, for more accurate phase noise modeling, the widely used theoretical PSD phase noise formula, given by Eq. (2), needs to be refined based on the used hardware components and their configuration.

The plot of Fig. 5(c) displays the beat signal spectrum of a single up-ramp frame by using both the conventional FFT and the splitting periodogram process depicted in Fig. 4(b), where N_{split} is equal to 10. It is relevant to mention that AWGN noise is simulated and digitally added into the time-domain signal of these two PSD curves, resulting in an SNR of $14\,\mathrm{dB}$. In other words, the combined effect of phase and AWGN noises produces an overall spectrum noise level, with respect to the target peak, of $14\,\mathrm{dB}$. Comparing both curves in Fig. 5(c), it is evident that the splitting periodogram method effectively smooths and reduces the noise floor originated by AWGN, making it a more robust option under AWGN conditions.

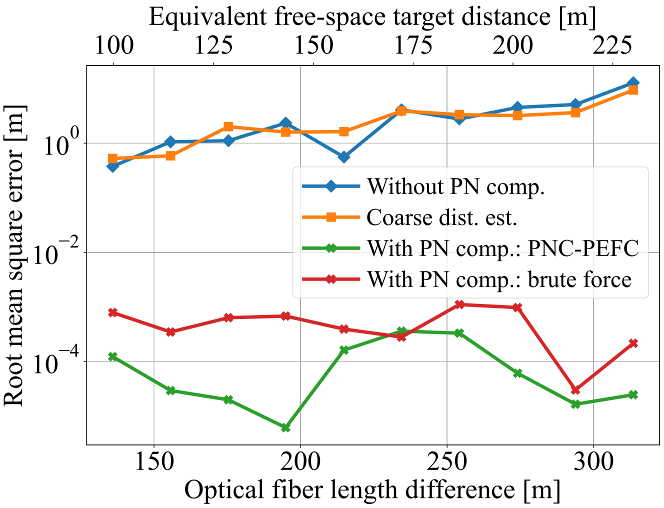

Fig. 6. Root mean square error (RMSE) of the distance estimation as a function of the optical fiber length difference in the target MZI for four different algorithms: (1) without phase noise compensation, employing the maximum peak of the FFT magnitude of the beat signal; (2) coarse distance estimator based on the periodogram splitting algorithm in Fig. 4(b); (3) with phase noise compensation utilizing the PNC-PEFC algorithm; and (4) with the brute force phase noise compensation algorithm proposed in [16].

As commented in Section III, the constant adjustable value α_{PN} of the PNC-PEFC algorithm plays an important role in the final phase noise compensation performance, and its effect is shown in Fig. 5(d). These curves are obtained by performing a periodogram of 10 up-ramp signals, with a target optical delay line of $280\,\mathrm{m}$. Examining the curves in Fig. 5(d), undesired additional peaks are emerging with a periodic separation proportional to the beat frequency of τ_m after phase noise compensation. The origin of these non-desired peaks is mainly due to the non-perfect IQ balance compensation within the PNC-PEFC algorithm. Moreover, the level of these undesired secondary peaks is proportional to the parameter k in Eq. (5). In other words, these peaks rise from phase noise extraction errors that accumulate during the phase noise extrapolation process described in Eq. (4).

These non-desired peaks can result in ghost targets and/or the inability to detect weak targets obscured by these undesirable peaks. Moreover, when increasing the α_{PN} value, two effects can be observed: an elevation of the non-desired frequency peak amplitudes, and a decrease of the compensated phase noise floor baseline. As an example, when α_{PN} is equal to 1, the phase noise spectrum floor is minimal, but the non-desired secondary peaks are more pronounced compared to when α_{PN} is 0.7. Therefore, there is a trade-off for the α_{PN} value. It is relevant to emphasize that the optimal value of α_{PN} can vary depending on τ_{tar} and the phase noise level of the FMCW optical signal.

The sweep of the τ_{tar} value shown in Fig. 6 is achieved by using different optical patch cords, resulting in a linear range of delay length differences in the target MZI from $136\,\mathrm{m}$ to $316\,\mathrm{m}$, with $20\,\mathrm{m}$ increments. The results are presented in terms of the root mean square error (RMSE) of the estimated distance.

Specifically, the figure compares four distance estimators: (1) without phase noise compensation; (2) coarse estimation applying the splitting periodogram method from Fig. 4(b); (3) the proposed phase noise compensation method from Fig. 4(a); and (4) the brute force phase noise compensation method proposed in [16]. When referring to the method without phase noise compensation, three blocks are applied in the following order: FFT, absolute value, and maximum peak detection (as shown by the blue blocks in Fig. 4(a)). Moreover, in Fig. 6, the equivalent target distance in free-space is indicated on the upper x-axis. Examining the blue and orange curves in Fig. 6, it can be observed that the RMSE of the estimated distance increases with the optical fiber length. This RMSE increase is due to the fact that the coherence between the two arms in the target MZI is inversely proportional to τ_{tar}, causing worse performance. In contrast, when applying the PNC-PEFC algorithm, the RMSE of the distance estimation remains approximately constant as the optical fiber length increases. Additionally, the brute force phase noise compensation method underperforms compared to the proposed PNC-PEFC technique. This is because the brute force approach selects the maximum FFT value from a set of compensated phase noise signals, and statistically, a phase noise compensated signal at a non-target distance may exhibit higher correlation than the phase noise compensated signal at the correct target distance [16]. As previously mentioned, the value of α_{PN} shows a trade-off between baseline phase noise compensation and undesired secondary peak levels. The level of these undesired secondary peaks is critical in multi-target scenarios where the dynamic range might be large. Since this study focuses on single-target detection, the value of α_{PN} is set to 1 to obtain the green and red curves in Fig. 6. Considering all the evaluated optical fiber lengths, the average mean absolute error (MAE) in distance estimation without phase noise compensation is $1.36\,\mathrm{m}$, whereas with the proposed phase noise compensation, it reduces to $0.88\,\mathrm{cm}$. These experimental results demonstrate an increase of more than two orders of magnitude in terms of distance estimation accuracy for detecting long-distance targets. To achieve an average error accuracy of $0.88\,\mathrm{cm}$, the FFT length is oversized by a factor of 10 for mitigating accuracy errors arising from the FFT bin width limitation. An interpolation process around the maximum FFT peak can be accomplished, which is a more efficient alternative than the oversized FFT approach.

As a final analysis, virtual AWGN noise is added in the time-domain to the digitized signal of the emulating target branch in Fig. 5(a) ($s_{tar}[n]$). A sweep of the SNR level is then conducted for all the evaluated optical fiber lengths. Then, for optimization purposes, a sweep of the N_{split} parameter is performed, yielding the detection probability results shown in Fig. 7. These results are obtained by employing the proposed PNC-PEFC algorithm. As seen in Fig. 7, detection probability improves when increasing N_{split}. This phenomenon occurs because the robustness against AWGN noise enhances as N_{split} increments. However, for N_{split} values higher than 480, the detection probability starts to deteriorate. This deterioration arises because the coarse distance estimation becomes less granular, resulting in less accurate phase noise compensation. Therefore, there is a trade-off in selecting N_{split}, with 480 being the optimal value for this experimental case. In Fig. 8, the probability of detection is calculated, taking into account that an error distance occurs when the estimated distance exceeds $5\,\mathrm{cm}$ compared to the actual distance (in terms of free-space propagation).

Once the optimized value of N_{split} is determined, the four previously discussed distance estimator methods are compared in Fig. 8. It is important to highlight that, for this experimental case, the proposed PNC-PEFC algorithm is ≈ 76 times more efficient in terms of number of complex multiplications than the brute force algorithm presented in [16]. Moreover, PNC-PEFC algorithm outperforms the brute force approach in terms of estimation accuracy for high SNR values, as corroborated

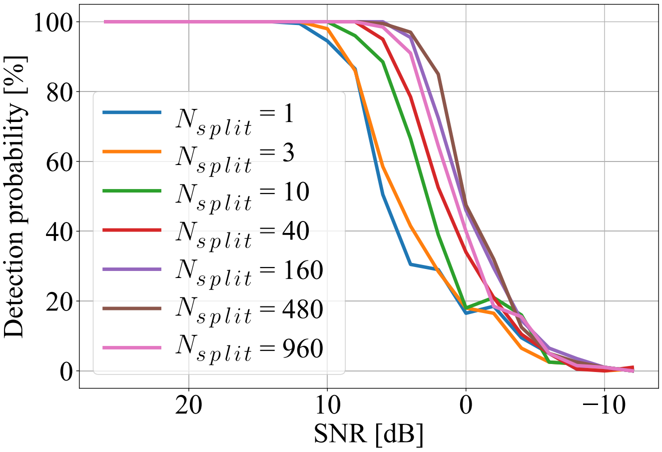

Fig. 7. Detection probability results as a function of the SNR level using the proposed PNC-PEFC algorithm for different values of N_{split}. The set distance error is $5\,\mathrm{cm}$, and the calculated detection probability considers all target distances in Fig. 6. Note: distance error refers to the maximum allowable deviation in distance measurement to qualify as an error, expressed in terms of free-space distance.

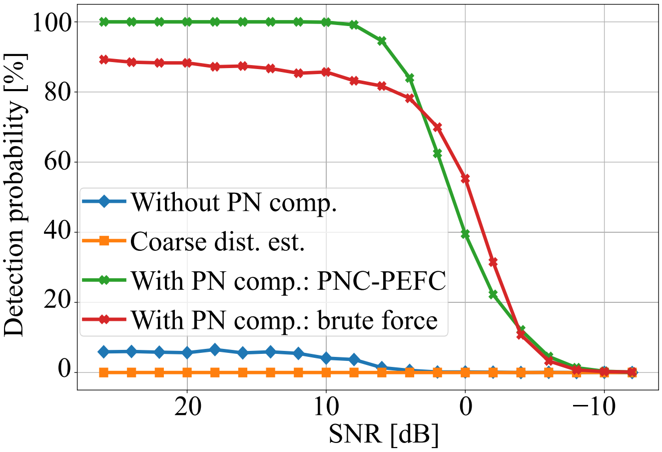

Fig. 8. Detection probability results as a function of the SNR level for four different algorithms, with a distance error of $5\,\mathrm{cm}$. Note: distance error refers to the maximum allowed deviation in distance measurement to qualify as an error and is in terms of free-space distance. These results are obtained by setting the value of α_{PN} to 1.

by the results in Fig. 6. As observed in Fig. 8, there is a significant improvement in detection probability performance when applying the proposed phase noise compensation method. Furthermore, as shown in the figure, both the method without phase noise compensation and the coarse distance estimation achieve a maximum detection probability below $10\,\%$ due to the phase noise impairment. In contrast, when the proposed PNC-PEFC phase noise compensation algorithm is applied, a $100\,\%$ detection probability is achieved at high SNR values. Specifically, at $10\,\mathrm{dB}$ SNR, the green curve in the figure begins to decay. This decay is primarily because of coarse distance estimator providing estimated distances with significant errors, thereby limiting the phase noise compensation performance, especially at low SNR values. Comparing with the brute force, the proposed PNC-PEFC algorithm shows better detection probability results at high SNR values due to more effective phase noise compensation. Nevertheless, below $\approx 2\,\mathrm{dB}$ SNR, the brute force algorithm performs better in terms of detection probability, as its performance does not depend on pre-coarse distance estimation. Hence, to further improve the PNC-PEFC algorithm, different strategies for this coarse distance estimation process can be explored.

In conclusion, the experimental results from Fig. 8 prove that the proposed PNC-PEFC algorithm offers excellent distance estimation performance under both phase noise and AWGN conditions. Hence, the PNC-PEFC algorithm is positioned as an enabling and promising solution for future automotive sensors based on FMCW LiDAR systems. For future work, more advanced phase noise compensation algorithms, operating under the same principles as PNC-PEFC, can be designed to cover multi-target and dynamic scenarios.

V. CONCLUSION

The manuscript first emphasized the potential of FMCW LiDAR sensors within the automotive industry, accelerating the path towards fully autonomous vehicles, where phase noise is highlighted as one of the most critical impairments. An overview of the current state-of-the-art solutions for phase noise compensation in automotive FMCW LiDAR systems was then presented, pointing out that the feedforward approach offers greater potential performance compared to the more widely used OPLL method. Furthermore, a research gap was identified in achieving effective phase noise compensation for automotive FMCW LiDAR sensors that balances high-performance, low-complexity, and robust reliability.

An analysis of phase noise in FMCW LiDAR systems was conducted, giving key aspects such as the origin of phase noise induced by the electrical noise of the laser driver. Moreover, a closed-form SNR formula was derived, integrating the two unavoidable drawbacks of FMCW LiDAR sensors: phase and shot noises. The proposed phase noise compensation PNC-PEFC algorithm based on feedforward correction was then introduced and explained, emphasizing its low-complexity and outlining key strategies for optimizing performance. In particular, the PNC-PEFC algorithm initiates with a coarse distance estimator which is robust against AWGN noise.

An experimental setup was built to evaluate the performance of the proposed PNC-PEFC algorithm across different target distances. Experimental results, in terms of RMSE of the distance estimation, were shown as a function of the target distance, comparing the performance with and without the PNC-PEFC algorithm. The performance of these two approaches was also presented in terms of detection probability, under varying SNR conditions. These experimental results clearly demonstrate a large performance improvement when applying the proposed PNC-PEFC algorithm under severe phase noise and AWGN conditions for long-distance targets. Additionally, the proposed algorithm allows for the use of relatively inexpensive lasers with broader linewidths, while minimizing the impact on overall system performance and reducing costs. As a conclusive remark, the proposed phase noise compensation PNC-PEFC algorithm is positioned as a key block for enabling the development of future FMCW LiDAR sensors in an efficient, low-cost, and reliable manner.

REFERENCES

[1] M. Martínez-Díaz and F. Soriguera, “Autonomous vehicles: Theoretical and practical challenges,” *Transp. Res. Procedia*, vol. 33, pp. 275–282, Oct. 2018.

[2] B. Behroozpour, P. A. M. Sandborn, M. C. Wu, and B. E. Boser, “LiDAR system architectures and circuits,” *IEEE Commun. Mag.*, vol. 55, pp. 135–142, Oct. 2017.

[3] S. Kuutti, S. Fallah, K. Katsaros, M. Dianati, F. Mccullough, and A. Mouzakitis, “A survey of the state-of-the-art localization techniques and their potentials for autonomous vehicle applications,” *IEEE Internet Things J.*, vol. 5, no. 2, pp. 829–846, Apr. 2018.

[4] R. Roriz, J. Cabral, and T. Gomes, “Automotive LiDAR technology: A survey,” *IEEE Trans. Intell. Transp. Syst.*, vol. 23, no. 7, pp. 6282–6297, Jun. 2022.

[5] H. Holzhüter, J. Bödewadt, S. Bayesteh, A. Aschinger, and H. Blume, “Technical concepts of automotive LiDAR sensors: A review,” *Opt. Eng.*, vol. 62, no. 3, Jan. 2023, Art. no. 031213.

[6] I. Bilik, “Comparative analysis of radar and LiDAR technologies for automotive applications,” *IEEE Intell. Transp. Syst. Mag.*, vol. 15, no. 1, pp. 244–269, Apr. 2023.

[7] M. Byeon and S. W. Yoon, “Analysis of automotive LiDAR sensor model considering scattering effects in regional rain environments,” *IEEE Access*, vol. 8, pp. 102669–102679, 2020.

[8] R. Ravindran, M. J. Santora, and M. M. Jamali, “Camera, LiDAR, and radar sensor fusion based on bayesian neural network (CLR-BNN),” *IEEE Sensors J.*, vol. 22, no. 7, pp. 6964–6974, Apr. 2022.

[9] K.-J. Boller et al., “Hybrid integrated semiconductor lasers with silicon nitride feedback circuits,” *Photonics*, vol. 7, no. 1, Dec. 2020, Art. no. 4.

[10] F. Ito, X. Fan, and Y. Koshikiya, “Long-range coherent OFDR with light source phase noise compensation,” *J. Lightw. Technol.*, vol. 30, no. 8, pp. 1015–1024, Apr. 2012.

[11] J.-Y. Ke et al., “Long distance high resolution FMCW laser ranging with phase noise compensation and 2D signal processing,” *Appl. Opt.*, vol. 61, no. 12, pp. 3443–3454, Apr. 2022.

[12] A. Binaie, S. Ahasan, and H. Krishnaswamy, “A spurless and wideband continuous-time electro-optical phase locked loop (CT-EOPLL) for high performance LiDAR,” *IEEE Open J. Solid-State Circuits Soc.*, vol. 1, pp. 235–246, Oct. 2021.

[13] B. Behroozpour et al., “Electronic-photonic integrated circuit for 3D microimaging,” *IEEE J. Solid-State Circuits*, vol. 52, no. 1, pp. 161–172, Jan. 2017.

[14] D. Dodane et al., “Optical phase-locked loop phase noise in 5G mm-wave OFDM ARoF systems,” *Opt. Commun.*, vol. 526, Jan. 2023, Art. no. 128872.

[15] Z. Yao, T. Mauldin, G. Hefferman, and T. Wei, “Digitally integrated self-trained predistortion curve finder for passive sweep linearization of semiconductor lasers,” *IEEE J. Sel. Topics Quantum Electron.*, vol. 25, no. 6, Nov./Dec. 2019, Art. no. 1502605.

[16] X. Zhang, “Laser chirp linearization and phase noise compensation for frequency-modulated continuous-wave LiDAR,” University of California, Berkeley, Apr. 2021.

[17] S. Banzhaf and C. Waldschmidt, “Phase-coded FMCW LiDAR,” in *Proc. 29th Eur. Signal Process. Conf.*, Dublin, Ireland, Dec. 2021, pp. 1775–1779.

[18] S. Venkatesh and W. Sorin, “Phase noise considerations in coherent optical FMCW reflectometry,” *J. Lightw. Technol.*, vol. 11, no. 10, pp. 1694–1700, Oct. 1993.

[19] A. Vasilyev, “The optoelectronic swept-frequency laser and its applications in ranging, three-dimensional imaging, and coherent beam combining of chirped-seed amplifiers,” Ph.D. dissertation, California Institute of Technology, May 2013.

[20] X. Zhang, J. Pouls, and M. C. Wu, “Laser frequency sweep linearization by iterative learning pre-distortion for FMCW LiDAR,” *Opt. Exp.*, vol. 27, pp. 9965–9974, Apr. 2019.

[21] M. P. Yankov, T. Fehenberger, L. Barletta, and N. Hanik, “Low-complexity tracking of laser and nonlinear phase noise in WDM optical fiber systems,” *J. Lightw. Technol.*, vol. 33, no. 23, pp. 4975–4984, Oct. 2015.

[22] H.-G. Ryu and Y.-S. Lee, “Phase noise analysis of the OFDM communication system by the standard frequency deviation,” *IEEE Trans. Consum. Electron.*, vol. 49, no. 1, pp. 41–47, Feb. 2003.

[23] DFB1550P, “1550nm, 100mW DFB butterfly laser with isolator, PM fiber,” Thorlabs, 2022. [Online]. Available: https://www.thorlabs.com/drawings/efa31ec98636cb21-A10CC158-EE22-DEA0-FE24A5A1283AF3CA/DFB1550P-SpecSheet.pdF

[24] S. Golestan, M. Monfared, F. D. Freijedo, and J. M. Guerrero, “Performance improvement of a prefiltered synchronous-reference-frame PLL by using a PID-Type loop filter,” *IEEE Trans. Ind. Electron.*, vol. 61, no. 7, pp. 3469–3479, Jul. 2014.

[25] X. Fan, Y. Koshikiya, and F. Ito, “Phase-noise-compensated optical frequency domain reflectometry with measurement range beyond laser coherence length realized using concatenative reference method,” *Opt. Lett.*, vol. 32, no. 22, pp. 3227–3229, Nov. 2007.

[26] S. Zhou and L. Rongfang, “Efficient and accurate frequency estimator under low SNR by phase unwrapping,” *Math. Problems Eng.*, vol. 2019, no. 1, Apr. 2019, Art. no. 7396074.

[27] H. Chen et al., “Interpolation linearization predistortion technology for FMCW LiDAR,” *Appl. Opt.*, vol. 63, pp. 1538–1545, Feb. 2024.